Photonic-digital hybrid artificial intelligence hardware architectures: at the interface of the real and virtual worlds

Journal of Physics: Photonics

PAPER

Photonic-digital hybrid artificial intelligence hardware architectures: at the interface of the real and virtual worlds

Lília M S Dias[1,2,3], **Dinis O Abranches**[4], **Ana R Bastos**[2], **Lianshe Fu**[1,*], **Albano N Carneiro Neto**[1], **Rui F P Pereira**[5], **Verónica de Zea Bermudez**[6], **Elias Towe**[3], **Rute A S Ferreira**[1,*] and **Paulo S B André**[2,*]

[1] Department of Physics and CICECO—Aveiro Institute of Materials, University of Aveiro, 3810-193 Aveiro, Portugal
[2] Department of Electrical and Computer Engineering and Instituto de Telecomunicações, Instituto Superior Técnico, Universidade de Lisboa, 1049-001 Lisbon, Portugal
[3] Department of Electrical and Computer Engineering, Carnegie Mellon University, Pittsburgh, PA 15213, United States of America
[4] CICECO—Aveiro Institute of Materials, Department of Chemistry, University of Aveiro, 3810-193 Aveiro, Portugal
[5] Chemistry Centre, University of Minho, 4710-057 Braga, Portugal
[6] Chemistry Department and CQ-VR, University of Trás-os-Montes e Alto Douro, Vila Real, Portugal
[*] Authors to whom any correspondence should be addressed.

E-mail: lianshefu@ua.pt, rferreira@ua.pt and paulo.andre@lx.it.pt

Keywords: hardware architecture, photonic layer, Gaussian process

Supplementary material for this article is available online

OPEN ACCESS

RECEIVED
26 June 2025

REVISED
31 July 2025

ACCEPTED FOR PUBLICATION
29 August 2025

PUBLISHED
10 September 2025

Abstract

Artificial intelligence (AI) technology has become an undeniable presence in society, as seen in the growing use of chatbots (e.g. ChatGPT) and recent Nobel Prize awards. However, the challenge of developing AI hardware architectures that efficiently integrate real-world analog signals with digital computational frameworks remains unresolved. This is particularly true for optical and neuromorphic computing systems. This work reports the implementation of an optical computing module in two hybrid AI architectures. The key element of the module is a photonic layer comprised of nanometer-scale spherical carbon dots. When excited with light-emitting diodes, the photonic layer exhibits a complex optical response. This layer is a feasible building block for two hybrid AI architectures: one based on optical processing and the other on the principles of neuromorphic computing. The modality of operation of the photonic layer is that it converts numerical input into a complex emission space, the results of which are processed using a Gaussian process model. Two systems based on this building block have been tested on a real-world dataset. They outperform conventional digital-only models, with coefficients of determination of $r^2 = 0.90$ and $r^2 = 0.84$ (training) and $r^2 = 0.85$ and $r^2 = 0.87$ (testing) for the optical and neuromorphic architectures, respectively. The systems discussed in this work serve as interfaces that bridge the real and virtual worlds. They offer exceptional optical properties, relative innocuity, low toxicity, stability, cost-effectiveness, seamless scalability, and robustness. The proposed architectures push the boundaries of advanced hybrid designs.

1. Introduction

With ever-increasing demand for more efficient data processing and real-time decision-making, traditional digital hardware architectures face significant bottlenecks in speed, scalability, and power consumption [1]. These needs are particularly acute with the rise of artificial intelligence (AI), where machine learning (ML) models process large volumes of data, requiring exceptional computational power [2]. This need is evident not only in the widespread use of the ChatGPT software application, developed by OpenAI, but also in advanced scientific calculations, such as those recognized with the Nobel Prizes in Physics and Chemistry in 2024, which were, respectively, for foundational discoveries and inventions that enabled ML with artificial neural networks (ANNs) [3, 4] and contributions to unraveling the complexities of proteins [5, 6]. Conventional computers based on the von Neumann architecture are inefficient for complex and adaptive

ML models [7]. The slowing of scaling according to Moore's law [8, 9] means there will be significant challenges for electronic hardware to increase computational bandwidth while reducing energy consumption; these challenges are emerging as critical bottlenecks that require alternative solutions beyond electronics [10].

Optical computing is an alternative active area for potentially efficient processing of large volumes of data at high rates [11]. This approach, however, has not yet reached a viability level as a replacement for conventional electronic computers [12]. Instead, special-purpose photonic hardware as AI computational accelerators opens up new frontiers in the form of neuromorphic engines [7]. Current approaches to all-optical processing require complex and high-energy-consuming components, which limit their scalability and practical application [10]. Examples include the use of optical memristors [13, 14] for integrated logic functions [15], and artificial synapses [16] with tunable features [17–19], envisioned for neuromorphic computing [20–22]. Other examples relate to photonic ANNs [23, 24] with memory features [25, 26] and single processing units [27] for neuromorphic computing [28], and optical communications [29]. The option of a hybrid solution that combines optics and digital processing with potentially low-energy consumption remains unexplored. We address it through a photonic–digital hybrid system for enhancing an AI accelerator architecture that leverages the unique properties of light. Our basic optical building block consists of various color light-emitting diodes (LEDs) pumping a photonic layer comprised of nanometer-scale spherical carbon dots (CDs), whose emission is analyzed by a spectrometer. The digital processor takes complex spectral-based responses generated by the photonic layer as input. The optical properties of the CDs are tunable through surface functionalization that enables unique emission characteristics when excited with light in the UV/visible spectral range [30].

Two photonic–digital hybrid AI architectures are demonstrated: one with a digital ML model based on a Gaussian processes (GPs), and another based on the principles of neuromorphic computing. The photonic layer maps a numerical input into a complex space derived from the emission properties. The result is fed into a ML model based on GP. The performance of both architectures surpasses that of the digital model operating alone in the training and testing stages. The photonic layer is a key component for the proposed low-power AI hardware architectures that combine an optical module with an advanced GP-based ML model.

2. Results

2.1. The photonic layer

To effectively perform optical computation, the photonic layer was designed to transform photonic stimuli from single peak emission LEDs, whose energy is down-shifted into characteristic emission spectra that depend on the selected individual LEDs or a combination of multiple LEDs. One key property of the photonic layer is the unpredictability of the emission spectra that should arise from complexity [31] that will provide the expanded complex representations (intermediated inputs) in the photonic–digital hybrid AI architectures. To ensure unpredictable emission spectra, three distinct families of single-component CDs with complementary spectral light harvesting and emission features were selected, and combined to produce multi-component CDs, whose photoluminescence spectra result from a complex superposition of the single-component ones [30]. This unpredictability arises from the random distribution of CDs within the matrix and their complex interactions (e.g. non-radiative energy transfer) [32],which fundamentally governs the resulting emission features and precludes the establishment of a reliable predictive model for the photonic layer emission behavior.

The single-component naphthalene-2,6-dicarboxylic acid CDs (labeled as NDCA-CDs, FL-CDs, and RhB-CDs) were synthesized by calcination of boric acid (BA) at 230 °C in the presence of NDCA, fluorescein (FL) and rhodamine B (RhB), respectively. The resulting CDs with sizes of 3–4 nm embedded in B_2O_3 matrix were structurally characterized as described in detail (figures 1(a) and S1–S3, supplementary information). The UV−visible absorption spectra (figure S3, supplementary information) show the main absorptions at 242 nm for NDCAs-CDs, 232 and 462 nm for FL-CDs, and 555 nm for RhB-CDs. The single-component CDs reveal a bright emission visible to the naked eye (figure 1(a)) that depends on the surface organic functionalization with NDCA, FL, and RhB. Their emission color crosses the Commission Internationale d'Éclairage (CIE) diagram spanning from the purplish-blue (NDCA-CDs), to the green (FL-CDs) and the yellow (RhB-CDs) spectral regions with (x,y) color coordinates of (0.18,0.14), (0.25,0.48) and (0.50, 0.47), respectively (figures 1(a) and (e)). The distinct color arises from the broad emission spectra (figure 1(f)), whose energy and full-width-at-half-maximum (FWHM) are independent of the excitation wavelength, indicating the presence of homogenous surface states embedded in the B_2O_3 matrix (figures S4–S6, supplementary information). Their excitation spectra (figure 1(g)) show broad bands with distinct components whose energy and FWHM depend on the surface modification. Based on these

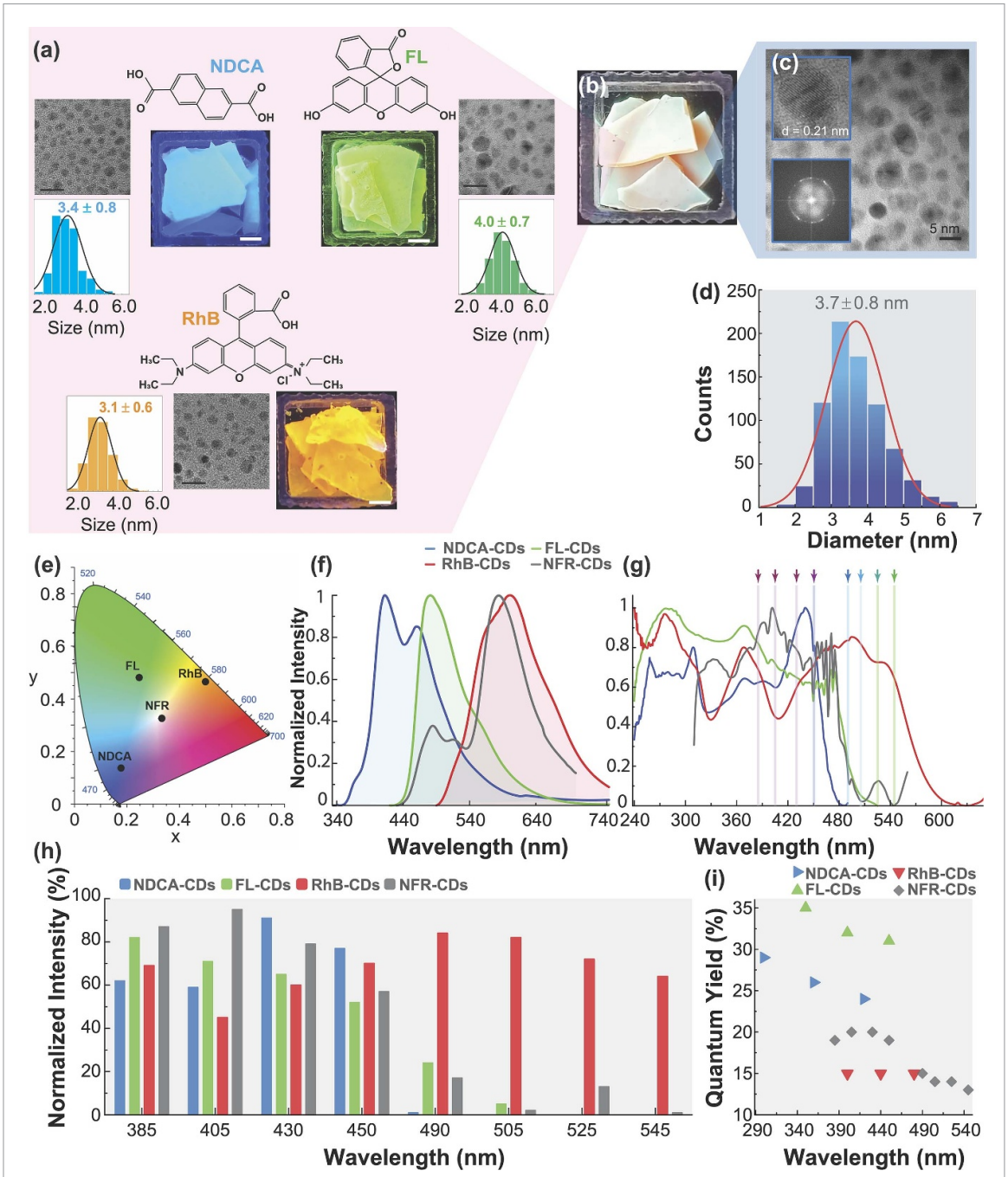

Figure 1. Characterization of the photonic layer. (a) Molecular structures of the organic molecules NDCA, FL, RhB; photographs (1×1 cm^2) under UV excitation of 365 nm, TEM images and nanoparticle size distributions of the corresponding CDs; (b) photograph (1×1 cm^2) of the triple-functionalized CDs (NFR-CDs) excited at 365 nm; (c) TEM image, and (d) nanoparticle size distribution [30]; (e) CIE chromaticity diagram with identified color coordinates of the NDCA-CDs, FL-CDs, RhB-CDs and NFR-CDs; (f) emission spectra of the CDs excited at 320 nm (NDCA-CDs), 400 nm (FL-CDs), 460 nm (RhB-CDs) and 410 nm (NFR-CDs); (g) excitation spectra of CDs monitored at 510 nm (NDCA-CDs), 550 nm (FL-CDs), 680 nm (RhB-CDs) and 585 nm (NFR-CDs [30]) with the excitation wavelengths of the LEDs 1–8 (wavelengths 385, 405, 430, 450, 490, 505, 525 and 545 nm, respectively) used to excite the NFR-CDs; (h) percentage of the maximum excitation intensity for the wavelengths of LEDs 1–8 and (i) QY as a function of the excitation wavelength for NDCA-CDs, FL-CDs, RhB-CDs and NFR-CDs.

single-component CDs with distinct and complementary spectral features, the photonic layer was designed combining all the surface modifiers into multi-component CDs (NFR-CDs) comprising spherical nanoparticles with 3.7 ± 0.8 nm and a highly crystalline structure analogous to graphene and an interplanar spacing of ~0.21 nm [30] (figures 1(c) and (d)). The NFR-CDs display white light emission (figures 1(b) and (e)) arising from the relative contribution observed for the single-component CDs, namely the emission spectra peak at 485 and 520 nm (from NDCA-CDs and FL-CDs, respectively) and 585 nm (from RhB-CDs) with different relative intensities (weights) (figure 1(f)).

Notably, when combined in a single sample, the optical features of the NFR-CDs comprise a complex superposition arising from changes in the individual radiative and non-radiative mechanisms. This complex

response is experimentally observed in the analysis of the excitation spectra, presenting different peaks in a broad spectral range and not resulting from the linear combination of the single-component ones. This is evident in figure 1(h), which shows the relative contribution of the excitation intensity as a function of selected excitation wavelengths employed as optical stimuli (385–545 nm). Under excitation at 385 nm, the relative absorption varies from around 62% for the NDCA-CDs to 87% for the NFR-CDs. At 405 nm, the NFR-CDs absorption is nearly resonant (95%) with the maximum excitation spectra, while the single-component CDs decrease for values between 45% and 71%. Upon further increasing the excitation wavelength, at 430 nm, the NDCA-CDs absorb around 90%, while the FL-CDs, RhB-CDs, and NFR-CDs show values between 60 and 79%. At 450 nm, the absorption ranges from 52% to 77%. For longer wavelengths (490–545 nm), the distinction between CDs becomes even more significant, as NDCA-CDs achieve their minima, followed by the FL-CDs, while, in contrast, the RhB-CDs achieve values close to their maximum (∼84%). This shows that whereas NDCA-CDs and FL-CDs determine the behavior of the NFR-CDs in the entire spectral range, the RhB-CDs mainly contribute at longer excitation wavelengths.

Another piece of evidence for complexity arises from the emission quantum yield (QY) dependence on the excitation wavelength. The QY is a key parameter as it determines the number of down-shifted photons per incident one for each excitation LED. Such ratio between the number of emitted photons to that of absorbed ones differs considerably for each sample and also with the excitation wavelength (figure 1(i)). The FL-CDs present the highest values 35% (350 nm), 32% (400 nm) and 31% (450 nm), followed by the NDCA-CDs with values of 29% (300 nm), 26% (360 nm) and 24% (420 nm), and RhB-CDs with 15% (400, 440 and 480 nm). When combined in the NFR-CDs, the QY is lower than those from the independent NDCA-CDs and FL-CDs, with values of 19% (385 nm and 450 nm), 20% (405 and 430 nm), 15% (490 nm), 14% (505 and 525 nm) and 13% (545 nm). In the latter case, a higher variation of the QY for different wavelengths is observed. When the emitting centers do not interact, the QY of a mixture can be estimated as a weighted average of the individual QYs, based on the proportion of each emitter. For example, Lipa *et al* [33] prepared PMMA polymer films containing coordination compounds of various lanthanide (Ln^{3+}) ions (Eu^{3+}, Tb^{3+}, Sm^{3+}, and Dy^{3+}), where each Ln^{3+} ion serves as an emitting center interacting only locally with its coordinating ligands. Because the Ln^{3+} ions do not interact, the QY of a mixed system can be predicted by calculating the weighted average of the individual QY of each Ln^{3+} complex in PMMA, according to their respective concentrations. For instance, in a sample composed of 10% Eu^{3+}, 10% Tb^{3+}, 45% Dy^{3+}, and 35% Sm^{3+}, the measured overall QY was 19%, which matched the estimated value derived from the individual QY of each component (QY = 85% for Eu^{3+}, 66% for Tb^{3+}, 6% for Dy^{3+}, and 3% for Sm^{3+}).

The photonic layer, composed of multi-component NFR-CDs, exhibits excitation-dependent emission, determined by the varying spectral contributions and energy conversion efficiencies. These characteristics result in complex emission responses under multi-wavelength excitation [30]. The complexity of the emission features may be interpreted as a fingerprint of the emergence of complex collective behavior in the NFR-CD chemical system [34]. The judicious mixture of the three types of CDs (NDCA-CDs, FL-CDs, RhB-CDs) yielded a synergistic behavior beyond the sum of the behavior of the individual CDs [31]. Interestingly, to produce the NFR-CDs system, we took advantage of the chemistry methods of the three types of individual CDs used as building blocks [35]. In the complex NFR-CDs system, the overall photoluminescent properties depend on intricate processes that occur on various scales in its building blocks (NDCA-CDs, FL-CDs, RhB-CDs) in a nontrivial way, since the laws that describe these properties are qualitatively diverse from those that govern the behavior of the individual ones [36].

The complex features of the photonic layer will be exploited as responses for optical computing, specifically for converting a numerical input into an enriched response with additional information from the physical properties of the layer, derived from its emission spectra. To that purpose, the emission spectra were measured under multi-excitation from the possible combinations of the 8 LEDs [30], S_X, with X being the integer value that is converted to 8-bit binary array representing the on ('1') or off ('0') states of each LED, respectively (tables S1 and S2, supplementary information), resulting in 256 distinct emission spectra (figure 2(a)). The emission spectra for selected stimuli (figure 2(b)) are shown in figure 2(d), revealing the spectral overlap of the NFR-CDs intrinsic emission (figure 1(f)) and the LEDs emission. To ensure that the photonic layer response is independent of the excitation source and to eliminate absolute intensity dependence on the experimental conditions, only the 568–683 nm spectral range (figure 2(e)) was considered. Moreover, the spectra were normalized to their maximum values to correct for LED intensity variations. This methodology enabled the implementation of two optical computing modules that convert numerical inputs into complex emission intermediate inputs for training and prediction in a digital ML model.

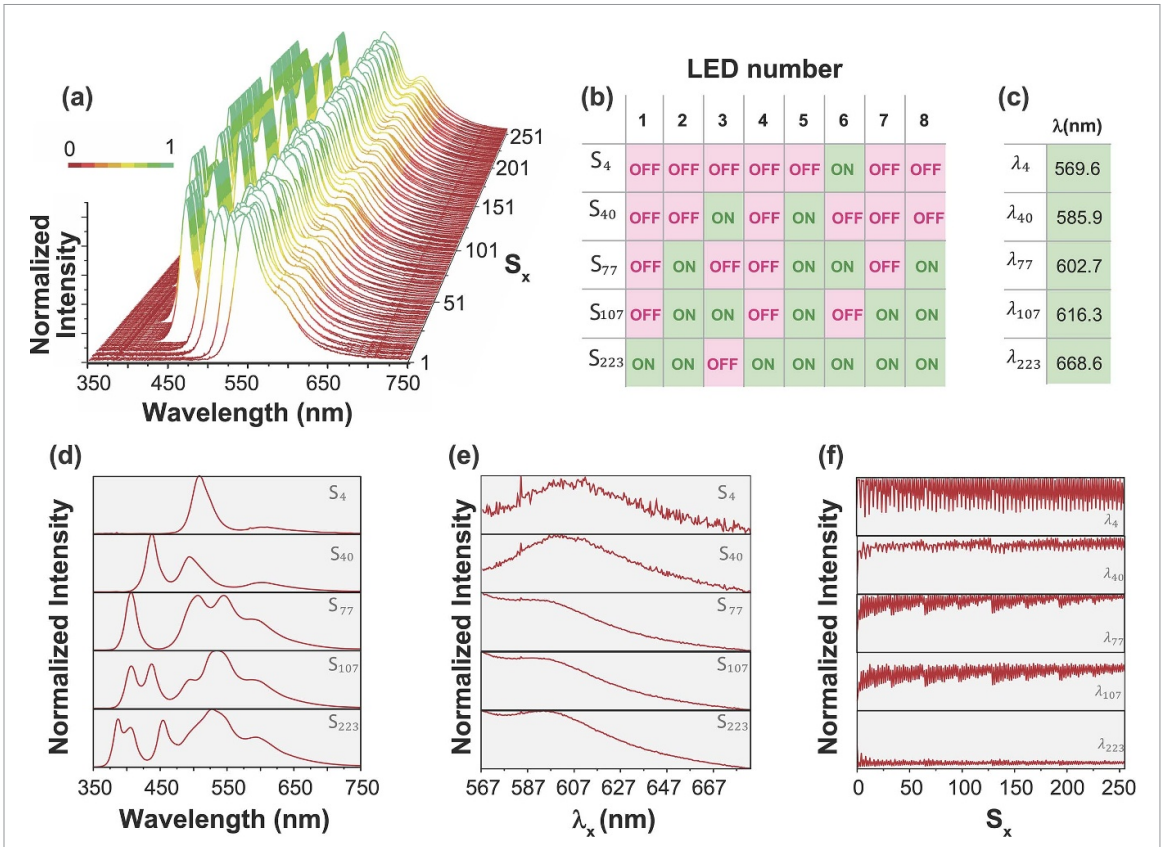

Figure 2. Optical responses of the photonic layer. (a) Emission spectra of the photonic layer under multi-excitation from the stimuli resultant of the combination of 8 LEDs (S_X, for $X > 0$); conversion of exemplificative integer inputs $X = 4$, 40, 77, 107 and 223, as (b) the combination of LEDs S_X or (c) a monitored wavelength λ_X; correspondent emission spectra for the selected conditions S_X in the (d) complete spectral range and (e) in the range selected as optical response (568–683 nm); (f) normalized intensity as a function of the LED combination S_x for selected monitored wavelengths λ_X.

2.2. Optical computing architecture

The principle and implementation scheme of the hybrid photonic–digital computing architecture proposed is illustrated in figure 3(a), comprising an optical computing module and a digital processing model. A numerical input (X) is first encoded as a superposition of light signals generated through the combination of the LEDs (S_x) with different emitting wavelengths. This signal is fed into the photonic layer consisting of the advanced optical material described above, which shows distinct emission responses to different excitation wavelengths (figure 2(e)). From the interaction between the light signal and the photonic layer results a complex and abstract intermediate representation, akin to the output of a typical neural network dense layer but generated at the speed of light without the need for costly computation steps. This intermediate signal (i.e. the emission spectrum) is then processed by the digital layer (GP model), yielding the final output (Y).

The performance of the hybrid computing architecture was tested using a real-world dataset related to auto insurance indicators (Swedish Auto Insurance [37]). This dataset was selected due to its numerical simplicity and small data features and labels, while maintaining real-world complexity. The dataset represents a count histogram of insurance claim payments made in thousands of Swedish Kronor (figure S7, supplementary information). Inputs (features) represent the number of insurance claims within a given payment bin, and outputs (labels) represent the value of that payment bin [37]. The full dataset contains 63 individual data points, which, following standard practices in the ML literature [38, 39], was split into independent training (75%) and testing (25%) datasets. The results obtained by fitting either the hybrid architecture to this dataset or only the GP without the intervention of the photonic layer are reported in figures 3(b) and (c), respectively.

Remarkably, the hybrid architecture outperforms the GP model for the dataset, yielding training and testing set coefficients of determination (r^2) of 0.90 and 0.85, respectively, superior to the figures obtained without the photonic layer (0.83 and 0.84, respectively). The intervention of the photonic layer improves the training and testing stages with the higher advantage seen in the training, as also inferred from the mean absolute error (MAE), in which the hybrid system yields MAE= 20.96 in the training and MAE=30.24 in the testing, while the GP model without the photonic layer results in MAE values of 27.00 and 31.91, respectively. As shown in figure 3(b), there is much less dispersion (i.e. the predicted and expected values are closer to

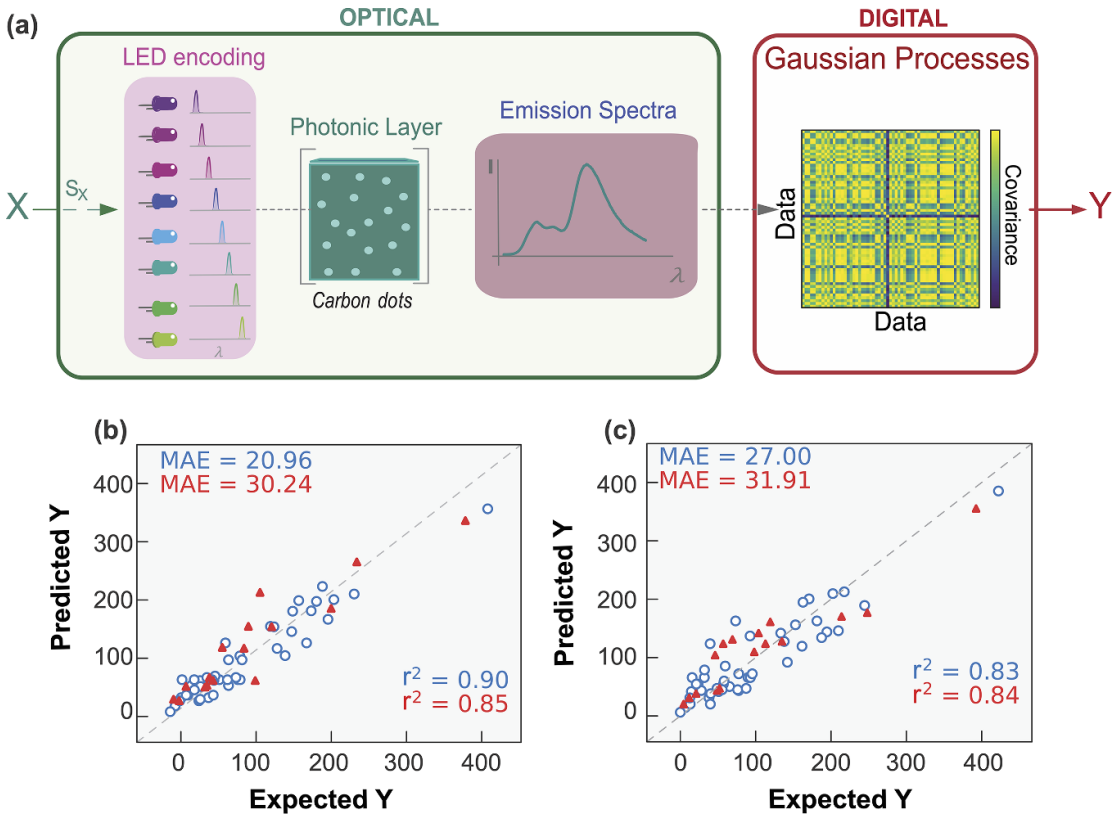

Figure 3. Optical computing architecture. (a) Hybrid architecture for optical computing composed of an optical computing module (left) and a digital model (right). The optical module consists of the encoding of an input X into the superposition of optical signals generated through the combination of the LEDs (S_x) used to excite the photonic layer, generating a response (emission spectrum). This spectrum enters the digital model that consists of a GP represented by its covariance matrix, generating an output Y. ((b), (c)) Expected versus predicted output for the training (blue circles) and testing (red triangles) stages using (b) the hybrid architecture and (c) the standalone GP. The line is a visual guide (Expected Y = Predicted Y).

each other and to the visual line guide) in the parity plot of our novel architecture over that of the individual GP. In both cases, there are no outlier points. This demonstrates the valuable contribution and effectiveness of the optical computing module in the hybrid architecture to enhance ML models' performance.

2.3. Optical neuromorphic architecture

The hybrid architecture discussed so far relies on the direct encoding of a numeric input into a combination of LEDs. While simple and efficient, this choice of encoding limits the number of independent data points to 2^N values, where N is the number of LEDs available. A variant of this architecture can be envisioned where each input value is mapped to a specific monitored wavelength (λ_X, with X being the numerical input) within the emission spectrum (figures 4(a) and table S3, supplementary information), making the input range only dependent on the spectral resolution and acquisition range. The photonic layer encodes a single input value as the intensity at λ_X, across all the spectra (figure 2(a)), as exemplified in figures 2(c) and (f). If the layer is excited at a fixed S_X, it will encode the input value as a single emission intensity at the mapped wavelength. Regardless of the input range and resolution of the spectrum, the lowest input value corresponds to the minimum monitored wavelength and the maximum input value to the highest monitored wavelength. The resultant emission intensities are processed by the GP model, retrieving a single output value (Y).

Besides fitting in the broad area of optical computing, this architecture aligns perfectly in the domain of neuromorphic engineering. This architecture resembles the functioning of an ANN built of 2^N neurons that correspond to the possible stimuli for the photonic layer (figure 4(b)). When an input value (X) is fed to the network, the state of all the neurons is computed as the intensities at the selected λ_X and enters the last node (GP) to obtain the output value (Y). This projected network is, in a way, trainable as the simple addition of one LED would double the number of neurons in the network, therefore increasing its complexity and robustness. This hybrid neuromorphic architecture yields a performance of r^2=0.84 in the training, and r^2=0.87 in the testing (figure 4(c)), respectively corresponding to MAE of 25.37 and 28.54. The effectiveness of the hybrid architecture was once again evaluated by comparing it with the performance of the GP without the intervention of the photonic layer (0.83 and 0.84 in the training and testing, respectively, figure 3(c)).

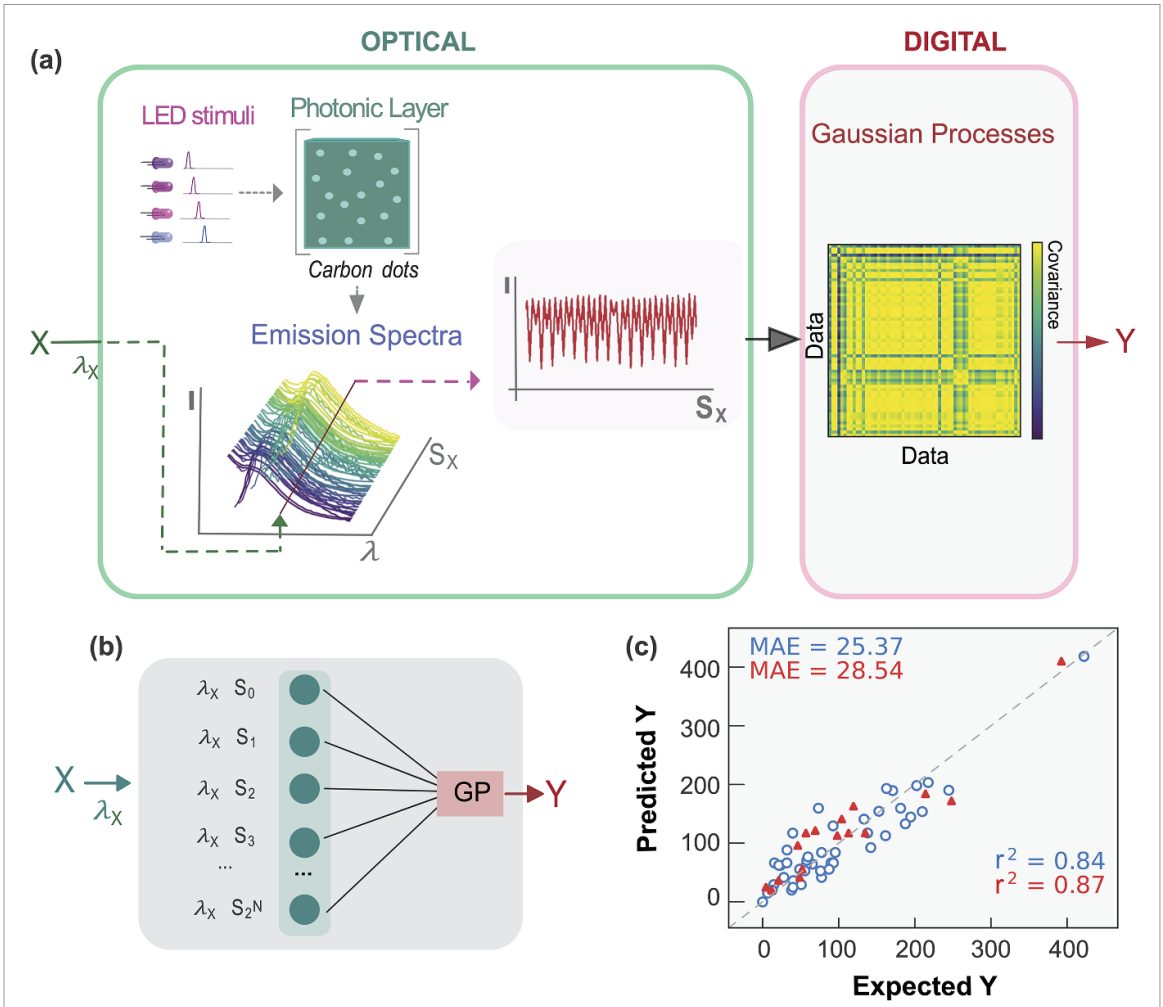

Figure 4. Optical neuromorphic architecture. (a) Hybrid optical neuromorphic architecture composed of an optical module (left) and digital model (right). In the optical module, LEDs are used to excite the photonic layer, generating a set of emission spectra from which an input X can be encoded as the intensity at a selected monitoring wavelength (λ_X) across all the spectra; this response enters the digital GP model represented by its covariance matrix, generating an output Y; (b) Scheme of the correspondent ANN architecture. (c) Expected versus predicted output for the training (blue circles) and testing (red triangles) stages using the hybrid neuromorphic architecture. The line is a visual guide (Expected Y = Predicted Y).

Similarly, to the previous architecture, the performance of the hybrid system is better than that of the digital GP both in the training and testing, but in this case the higher improvement is in the testing stage.

3. Discussion

In both architectures, optical data from the photonic layer is processed using a GP model [40]. While alternative models such as ANNs could be considered, GPs are non-parametric, with few hyperparameters, fast training, and excellent performance with limited data [41]. Crucially, retraining requires only an update to the covariance matrix, with no need for batch-wise optimization or re-tuning. These features make GPs particularly well-suited for integration with photonic systems.

The optical computing architecture presents the versatility that includes a sequential conversion from the single integer input value into a binary array that comprises the states of N LEDs that are used to trigger an emission response from the photonic layer, generating a single emission spectrum that enters the digital ML model. This characteristic behavior enables the encoding of categorical data, as each of the possible input values has a corresponding fingerprint based on the generated spectrum. Although the number of employed LEDs limits the number of possible inputs, the simple addition of one LED can double the number of inputs. Through this architecture, the system was demonstrated as application-specific to be applied in datasets that obey certain conditions, namely the input values being integer numbers from 0 to $2^N - 1$. By proving the concept using a real-world dataset, the performance with the photonic layer surpassed the operation of the digital system alone, by an r^2 difference of 0.07 in the training set and 0.01 in the testing set.

Towards the generalization of the system, the input range may not depend on the number of LEDs, but on the resolution and spectral range of the emission spectrum. Therefore, in a proposed neuromorphic engineering approach, the encoded data is the emission intensity variation in the spectra at a specific monitored wavelength. Here, the usefulness of the system was once again demonstrated, with an improvement of the system performance when compared to the digital counterpart operating alone, by an r^2 difference of 0.01 in the training and 0.03 in the testing. This architecture is general and can be used in datasets where the inputs can range across any values. Furthermore, the complexity of the photonic layer can be enhanced by increasing the number of photonic stimuli, enabling a single input value to be encoded into multiple values. Although the number of possible input values is limited by the resolution and spectral range of the spectrum, this architecture offers greater flexibility, as this restriction can be altered by employing acquisition equipment with higher acquisition rates and/or larger spectral ranges.

The proposed hybrid architectures capitalize on the strengths of optical and digital computing domains, making it a competitive alternative to state-of-the-art solutions. While both architectures surpass the performance of the standalone digital ML model, demonstrating their usefulness, one yields its largest advantage in the training stage (optical computing architecture) and the other in the testing stage (optical neuromorphic architecture). Performance comparisons confirm that both architectures outperform the all-digital counterpart, which supports that photonic AI is one of the paths to take.

The results reported in this work would be surprising even if the hybrid AI architectures did not outperform the standalone GP models. Severe information loss is to be expected from the process of converting an input data point into a collection of emission spectra, followed by passing this amalgamated spectrum through a photonic layer characterized by its complex response. However, GPs effortlessly leverage this abstract spectral response as a feature set to obtain accurate predictions. That a physical photonic layer and a digital GP can work in unison and produce anything other than a scatter plot of unreliable predictions is intriguing. The size and numerical simplicity of the selected dataset allowed us to directly evaluate and validate the hybrid approach proposed in this work without having to resort to complicated feature conversion techniques to convert a multi-dimensional feature space to binary LED combinations. Having carried out the validation of the hybrid approach, feature conversion techniques can be employed in multi-dimensional inputs, as images, and in larger datasets as future work, where other ML models, such as ANNs, can also be evaluated. As far as we know, this is the first time that a hybrid photonic–digital AI implementation comprised of a physical photonic layer integrated with an advanced digital GP model is demonstrated. This integration is new and disruptive in the respective fields and significantly shows how photonics can be introduced in AI as a tool for information processing and prediction. This is a breakthrough for both fields of photonics and ML, as we have demonstrated a bridge between the physical and virtual worlds, paving the way for new research lines to evolve.

4. Methods

4.1. Photonic layer

4.1.1. Materials and synthesis

NDCA, FL, RhB, and BA were used as received. Ethanol (EtOH) was used as a solvent for the preparation of stock solutions for NDCA, FL, and RhB with concentrations of 2.0, 2.0, and 2.4 mg mL^{-1}, respectively.

Synthesis of single-component NDCA-CDs, FL-CDs, and RhB-CDs and multi-component NFR-CDs. 1.0 mg of NDCA (or 0.5 mg of FL or 0.05 mg of RhB) in EtOH was ground well with 1.0 g of BA to obtain a homogenous mixture, and then calcinated at 230 °C for 9 min, taken out from the oven, and cooled down to room temperature naturally. The resulting CDs are designated as NDCA-CDs, FL-CDs and RhB-CDs, respectively. The synthesis of multi-component CDs (NFR-CDs) was reported elsewhere [30]. Typically, a mixture of 1.0 mg of NDCA (0.5 mL of NDCA in EtOH, 2.0 mg mL^{-1}), 0.5 mg of FL (0.25 mL of FL in EtOH, 2.0 mg mL^{-1}) and 0.05 mg of RhB (0.021 mL of RhB in EtOH, 2.4 mg mL^{-1}) was ground well with 1.0 g of BA to obtain a homogenous mixture, and then calcinated at 230 °C for 9 min. The undoped BA was also heated, and the resulting product was designated as Heated-BA.

4.1.2. Characterization techniques

The TEM images were obtained using a JEOL JEM 2100 (200 kV) microscope. In 5 ml of water, 1.5 mg of each sample was dispersed and placed into the analyzing grids (UC-A on holey 400 mesh Cu grids, Ted Pella ref. 01824) by drop-casting and dried at room temperature. The photoluminescence spectra and emission QY were recorded as reported previously elsewhere [42]. All the measurements were conducted under ambient conditions over ∼10 months, during which the optical response remained stable, confirming both the long-term and batch-wise reproducibility.

4.1.3. Emission spectra under multi-excitation

The photonic layer based on NFR-CDs was excited with photonic stimuli from all the possible combinations of 8 LEDs with different wavelengths 385 nm (LED385L, ThorLabs), 405 nm (LED405L, ThorLabs), 430 nm (SMC430, Roithner LaserTechnik), 450 nm (LED450L, ThorLabs), 490 nm (LED490L, ThorLabs), 505 nm (LED505L, ThorLabs), 525 nm (LED525L, ThorLabs) and 545 nm (LED545L, ThorLabs), tables S1 and S2, supplementary information. The resultant emission spectrum for each excitation was measured using a portable spectrometer (OceanOptics Maya 2000 Pro), as reported elsewhere [30]. Only the spectral region from 568 to 683 nm was considered and normalized to the maximum, to minimize the excitation contribution in the spectrum and the influence of the LED intensity variability, respectively. As 8 light sources are used, there are 2^8 possible photonic stimuli resultant from their combination, and therefore 2^8 different emission spectra generated from the layer.

ML Model. The ML model employed consists of a GP [41]. For the ML validation, a standard dataset available online was used, consisting of the Swedish Auto Insurance Dataset [37] that has one feature (integer) and one label (decimal). Following common procedures in the ML literature, the dataset was split into training (75%) and testing (25%), with the former being the dataset used to train the model, and the latter used to evaluate the generalization capability of the model. The splitting was performed using an iterative stratified method, developed by Sechidis *et al* [43] and Szymanski and Kajdanowicz [44],where different training/testing combinations were attempted to ensure the training and testing sets are both representative of the data in the full database. Regardless of the architecture of the system, the input value from the dataset encoded in the photonic layer was fed into the GP model, which predicted an output. GPs were trained using the Radial-Basis Function kernel, here chosen due to its simplicity, a trainable likelihood (to handle experimental noise), and a null mean function. When working with the proposed hybrid architecture, the GP model also incorporated a convolutional kernel. The details of the GP model implementation are in supplementary information S2. The decision to incorporate a GP convolution kernel in the hybrid architectures was due to the spectral nature of the inputs, meaning that input dimensions (i.e. features) are not independent from each other but highly correlated. The selected patch size for the convolution was 32 bins, as it is a common value for inputs with 256 dimensions. The normalization for the features and labels is detailed in supplementary information S2 and S3 (tables S4–S6). A sweep was made with different normalization techniques, and the ones that yielded better r^2 in the training were selected. In all cases, normalizing the features with log-standardization and the labels with standardization yielded the best results.

Performance evaluation. To evaluate the performance of the hybrid architectures or the individual GPs, the employed metric was the coefficient of determination (r^2) between the actual (y) and the predicted outputs ($\hat{y}$), as given by equation (1), where $\bar{y}$ is the average of the actual values and n the number of points. A higher r^2 is indicative that the predictions are closer to the actual values. This metric was obtained both for the training and the testing sets, and for different types of normalization of features and labels (tables S4–S6, supplementary information),

$$r^2 = 1 - \frac{\sum_i^n (y_i - \hat{y}_i)^2}{\sum_i^n (y_i - \bar{y})^2}. \tag{1}$$

The MAE was calculated with equation (2),

$$\mathrm{MAE} = \sum_i^n \frac{|y_i - \hat{y}_i|}{n}. \tag{2}$$

Data availability statement

The data that support the findings of this study are available upon reasonable request from the authors.

Acknowledgments

This work was financed by Portugal 2020 through European Regional Development Fund (ERDF) in the frame of CENTRO2020 in the scope of the projects CICECO—Aveiro Institute of Materials, UIDB/50011/2020 (https://doi.org/0.54499/UIDB/50011/2020), UIDP/50011/2020 (https://doi.org/10.54499/UIDB/50011/2020) and LA/P/0006/2020 (https://doi.org/10.54499/LA/P/0006/2020) and Instituto de Telecomunicações, UIDB/50008/2020 (https://doi.org/10.54499/UIDB/50008/2020), UIDP/50008/2020 (https://doi.org/10.54499/50008/2020) and LA/P/0109/2020 (https://doi.org/10.54499/LA/P/0109/2020) financed by national funds through the FCT/MEC (PIDDAC) and when appropriate co-financed by FEDER under the PT2020 Partnership through European Regional Development Fund (ERDF) in the frame of Operational Competitiveness and Internationalization Programme (POCI). LMSD thanks FCT for the PhD grant (https://doi.org/10.54499/UI/BD/153491/2022). RFPP acknowledges FCT for the Strategic Funding UID/00686: Centro de Química da Universidade do Minho (CQ-UM/UM) and FCT-UMinho for the Assistant Research contract (https://doi.org/10.54499/2023.07994.CEECIND/CP2841/CT0013). ARB acknowledges the financial support from IT-Lisbon and FCT under Contract No. CEECINST/00058/2021/CP2816/CT0004.

Conflict of interest

The authors declare no competing interests.

Additional information

The online version contains supplementary material. Correspondence and requests for materials should be addressed to P S André or R A S Ferreira.

Author contributions

Lília M S Dias 0000-0001-8077-1355
Data curation (equal), Formal analysis (equal), Investigation (equal), Methodology (equal), Software (equal), Writing – original draft (equal), Writing – review & editing (equal)

Dinis O Abranches 0000-0003-0097-2072
Formal analysis (equal), Methodology (equal), Software (equal), Validation (equal), Writing – original draft (equal)

Ana R Bastos 0000-0002-3251-6306
Investigation (equal), Methodology (equal), Software (equal), Supervision (equal), Writing – original draft (equal)

Lianshe Fu 0000-0002-9887-371X
Investigation (equal), Methodology (equal), Validation (equal), Writing – original draft (equal)

Albano N Carneiro Neto 0000-0003-2432-0992
Formal analysis (equal), Methodology (equal), Writing – original draft (equal)

Rui F P Pereira 0000-0001-7279-5728
Methodology (equal), Formal analysis (equal), Writing – original draft (equal), Writing – review & editing (equal)

Verónica de Zea Bermudez 0000-0002-7577-4938
Formal analysis (equal), Writing – original draft (equal), Writing – review & editing (equal)

Elias Towe
Methodology (equal), Formal analysis (equal), Writing – original draft (equal), Writing – review & editing (equal)

Rute A S Ferreira 0000-0003-1085-7836
Conceptualization (equal), Data curation (equal), Formal analysis (equal), Funding acquisition (equal), Investigation (equal), Methodology (equal), Project administration (equal), Resources (equal), Software (equal), Supervision (equal), Validation (equal), Visualization (equal), Writing – original draft (equal), Writing – review & editing (equal)

Paulo S B André 0000-0002-6276-4976
Conceptualization (equal), Data curation (equal), Formal analysis (equal), Funding acquisition (equal), Investigation (equal), Methodology (equal), Project administration (equal), Resources (equal), Software (equal), Supervision (equal), Validation (equal), Visualization (equal), Writing – original draft (equal), Writing – review & editing (equal)

References

[1] McMahon P L 2023 The physics of optical computing *Nat. Rev. Phys.* **5** 717–34
[2] Garisto D 2024 How cutting-edge computer chips are speeding up the AI revolution *Nature* **630** 544–6
[3] Hopfield J J 1982 Neural networks and physical systems with emergent collective computational abilities *Proc. Natl Acad. Sci. USA* **79** 2554–8
[4] Fahlman S E, Hinton G E and Sejnowski T J 1983 Massively parallel architectures for AI: NETL, thistle, and Boltzmann machines *AAAI'83: Proc. 3rd AAAI Conf. on Artificial Intelligence* pp 109–13
[5] Baek M *et al* 2021 Accurate prediction of protein structures and interactions using a three-track neural network *Science* **373** 871–6
[6] Jumper J *et al* 2021 Highly accurate protein structure prediction with AlphaFold *Nature* **596** 583–9
[7] Shastri B J *et al* 2021 Photonics for artificial intelligence and neuromorphic computing *Nat. Photon.* **15** 102–14
[8] Moore G E 2006 Cramming more components onto integrated circuits, reprinted from electronics, volume 38, number 8, April 19, 1965, pp.114 ff *IEEE Solid-State Circuits Soc. Newsl.* **11** 33–35
[9] Theis T N and Wong H-S P 2017 The end of Moore's Law: a new beginning for information technology *Comput. Sci. Eng.* **19** 41–50
[10] Kudithipudi D *et al* 2025 Neuromorphic computing at scale *Nature* **637** 801–12
[11] Kibebe C G, Liu Y and Tang J 2024 Harnessing optical advantages in computing: a review of current and future trends *Front. Phys.* **12** 1379051
[12] Ambs P 2010 Optical computing: a 60-year adventure *Adv. Opt. Technol.* **2010** 1–15
[13] Youngblood N, Ríos Ocampo C A, Pernice W H P and Bhaskaran H 2023 Integrated optical memristors *Nat. Photon.* **17** 561–72
[14] Hu L, Yang J, Wang J, Cheng P, Chua L O and Zhuge F 2021 All-optically controlled memristor for optoelectronic neuromorphic computing *Adv. Funct. Mater.* **31** 2005582
[15] Tan H, Liu G, Yang H, Yi X, Pan L, Shang J, Long S, Liu M, Wu Y and Li R-W 2017 Light-gated memristor with integrated logic and memory functions *ACS Nano* **11** 11298–305
[16] Yang R, Wang Y, Li S, Hu D, Chen Q, Zhuge F, Ye Z, Pi X and Lu J 2024 All-optically controlled artificial synapse based on full oxides for low-power visible neural network computing *Adv. Funct. Mater.* **34** 2312444
[17] Zhu X and Lu W D 2018 Optogenetics-inspired tunable synaptic functions in memristors *ACS Nano* **12** 1242–9
[18] Zhang T, Fan C, Hu L, Zhuge F, Pan X and Ye Z 2024 A reconfigurable all-optical-controlled synaptic device for neuromorphic computing applications *ACS Nano* **18** 16236–47
[19] Wang Y, Yin L, Huang W, Li Y, Huang S, Zhu Y, Yang D and Pi X 2021 Optoelectronic synaptic devices for neuromorphic computing *Adv. Intell. Syst.* **3** 2000099
[20] Portner K, Schmuck M, Lehmann P, Weilenmann C, Haffner C, Ma P, Leuthold J, Luisier M and Emboras A 2021 Analog nanoscale electro-optical synapses for neuromorphic computing applications *ACS Nano* **15** 14776–85
[21] Marunchenko A, Kumar J, Kiligaridis A, Tatarinov D, Pushkarev A, Vaynzof Y and Scheblykin I G 2024 Memlumor: a luminescent memory device for energy-efficient photonic neuromorphic computing *ACS Energy Lett.* **9** 2075–82
[22] Zhu C *et al* 2022 Optical synaptic devices with ultra-low power consumption for neuromorphic computing *Light Sci. Appl.* **11** 337
[23] Xiang S *et al* 2024 Semiconductor lasers for photonic neuromorphic computing and photonic spiking neural networks: a perspective *APL Photonics* **9** 070903
[24] Bandyopadhyay S, Sludds A, Krastanov S, Hamerly R, Harris N, Bunandar D, Streshinsky M, Hochberg M and Englund D 2024 Single-chip photonic deep neural network with forward-only training *Nat. Photon.* **18** 1335–43
[25] Aguirre F *et al* 2024 Hardware implementation of memristor-based artificial neural networks *Nat. Commun.* **15** 1974
[26] Biasi S, Donati G, Lugnan A, Mancinelli M, Staffoli E and Pavesi L 2024 Photonic neural networks based on integrated silicon microresonators *Intell. Comput.* **3** 0067
[27] Meng X *et al* 2023 Compact optical convolution processing unit based on multimode interference *Nat. Commun.* **14** 3000
[28] Guo X, Zhou H, Xiang S, Yu Q, Zhang Y, Han Y, Wang T and Hao Y 2024 Experimental demonstration of a photonic reservoir computing system based on fabry perot laser for multiple tasks processing *Nanophotonics* **13** 1569–80
[29] Silva L C B, Marciano P R N, Pontes M J, Monteiro M E, André P S B and Segatto M E V 2025 Integrated photonic neural networks for equalizing optical communication signals: a review *Photonics* **12** 39
[30] Dias L M S, Fu L, Pereira R F P, Carneiro Neto A N, Bermudez V D Z, André P S and Ferreira R A S 2024 Evolving photonic authentication with sustainable luminescent smart e-tags *FlexMat* **1** 116–26
[31] Goldenfeld N and Kadanoff L P 1999 Simple lessons from complexity *Science* **284** 87–89
[32] Onishi B S D, Carneiro Neto A N, Bortolleto-Santos R, Masterlaro V R, Carlos L D, Ferreira R A S and Ribeiro S J L 2024 Carbon dots on LAPONITE® hybrid nanocomposites: solid-state emission and inter-aggregate energy transfer *Nanoscale* **16** 6286–95
[33] Lipa A, Pham Y H, Carneiro Neto A N, Trush V A, Li H, Malta O L, Amirkhanov V M and Gawryszewska P 2025 High emission quantum yields and color-tunable properties of Ln-chelates embedded in PMMA *J. Mater. Chem. C* **13** 2142–53
[34] Anderson P W 1972 More is different *Science* **177** 393–6
[35] Azevedo H S, Perry S L, Korevaar P A and Das D 2020 Complexity emerges from chemistry *Nat. Chem.* **12** 793–4
[36] Vicsek T 2002 Complexity: the bigger picture *Nature* **418** 131
[37] Bob R R 2022 Auto insurance in Sweden (available at: www.kaggle.com/datasets/rupakroy/auto-insurance?select=auto-insurance.csv)
[38] Artrith N, Butler K T, Coudert F-X, Han S, Isayev O, Jain A and Walsh A 2021 Best practices in machine learning for chemistry *Nat. Chem.* **13** 505–8
[39] Abranches D O, Maginn E J and Colón Y J 2023 Boosting graph neural networks with molecular mechanics: a case study of sigma profile prediction *J. Chem. Theory Comput.* **19** 9318–28
[40] Seeger M 2004 Gaussian processes for machine learning *Int. J. Neural. Syst.* **14** 69–106

[41] Abranches D O, Maginn E J and Colón Y J 2024 Stochastic machine learning via sigma profiles to build a digital chemical space *Proc. Natl Acad. Sci.* **121** e2404676121
[42] Silva S F V, Figueiredo G, Pereira R F P, de Zea Bermudez V, Fu L, André P S, Carneiro Neto A N and Ferreira R A S 2024 *Time-gated multi-dimensional luminescence thermometry* via carbon dots for precise temperature mobile sensing *Nanoscale* **16** 20532–41
[43] Sechidis K, Tsoumakas G and Vlahavas I 2011 On the Stratification of Multi-label Data *Machine Learning and Knowledge Discovery in Databases ECML PKDD 2011 (Lecture Notes in Computer Science)* ed D Gunopulos, T Hofmann, D Malerba and M Vazirgiannis, vol 6913 (Springer) pp 145–58
[44] Szymański P and Kajdanowicz T 2017 A network perspective on stratification of multi-label data (arXiv:1704.08756)